Ultrasmall Confined Iron Oxide Nanoparticle MSNs as a pH-Responsive Theranostic Platform

Meiying Wu, Qingshuo Meng, Yu Chen, Pengfei Xu, Shengjian Zhang, Yaping Li, Lingxia Zhang, Min Wang, Heliang Yao, and Jianlin Shi**

A unique mesoporous silica nanoparticles (MSNs)-based theranostic platform with ultrasmall iron oxide nanoparticles (NPs) confined within mesopore network has been developed by a facile but efficient physical-vapor-infiltration (PVI) method. The highly dispersed Fe species within mesopore channels can synchronously function as the non-toxic contrast agents for highly efficient T_1-weighted MR imaging, and as anchoring sites for anti-cancer drug molecule loading and pH-responsive release based on the special metal-ligand coordination bonding between the Fe species and drug molecules. Moreover, the obtained Fe-MSNs exhibit favorable biocompatibility, enhanced chemotherapeutic efficacy and concurrently diminished side effects due to the non-specific attack of chemotherapeutic drugs, as well as the capability in circumventing the multidrug resistance (MDR) of cancer cells and suppressing the metastasis of tumor cells in vitro and in vivo. This pH-resoponsive theranostic agent provides a new promising MSNs-based anti-cancer nanomedicine for future biomedical application.

1. Introduction

Cancer nanotheranostics which combine diagnostic probes and therapeutic agents in one carrier by means of nanobiotechnology have received widespread attention in recent years.[1] Such nanoscale theranostic systems have the potential to substantially improve current cancer therapies by noninvasive real time monitoring of the therapeutic progression in the pathological conditions. The complicated in vivo physiological environment needs more intelligent and multifunctional integrated theranostic nanosystems to achieve the desired diagnostic and therapeutic outcomes. Achieving "zero-release" of drugs from nanocarriers before reaching the desired cells or tissues is of great importance to concurrently minimize the systemic toxicity and enhance the therapeutic effect of therapeutic agents. Great efforts have been devoted to seeking effective approaches to address the above-mentioned toxicity and efficacy issues. The design of imaging-guided theranostic nanosystems with stimuli-responsiveness according to the physiological differences between cancerous and normal tissues, such as pH value,[2] redox environment,[3] temperature,[4] etc., will open new avenues for the development of intelligent biomedical platforms with controlled drug release properties under imaging guidances. Especially, these multifunctional nanomedicines should be endowed with following features: accurately diagnosing the local lesions, enabling the "zero premature drug release" before reaching the diseased sites, achieving an enhanced treatment efficacy once reaching focuses.

Magnetic resonance imaging (MRI) has become one of the most widely used diagnostic modality clinically, either because of its high spatial resolution and penetration depth for soft tissues, or due to its noninvasive and real-time monitoring features. T_1-weighted MRI (T_1-MRI) provides a bright signal compared with the dark background, resulting in improved detection accuracy.[5] Paramagnetic compounds including Gd^{3+}, Mn^{2+}, and Fe^{3+} have large numbers of unpaired electrons, thus they can be used as T_1 contrast agents (CAs).[6] It has been proven that the accessibility of water molecules to the paramagnetic centers is the key factor for enhancing the resolution and signal-to-noise of T_1-MRI.[7] Many material systems such as organic, inorganic and organic/inorganic hybrid nanoparticulate systems have been introduced in the nanotheranostics to enhance the efficacy of T_1-MRI,[8] among which biocompatible mesoporous silica nanoparticles (MSNs) have been considered as an excellent theranostic vehicle to address

Dr. M. Wu, Dr. Y. Chen, Dr. L. Zhang, Dr. M. Wang, Dr. H. Yao, Prof. J. Shi
State Key Laboratory of High Performance Ceramics and Superfine Microstructure
Shanghai Institute of Ceramics
Chinese Academy of Sciences
1295 Ding-Xi Road
Shanghai 200050, PR China
E-mail: jlshi@mail.sic.ac.cn
Dr. Q. Meng, Dr. P. Xu, Prof. Y. Li
Shanghai Institute of Materia Medica
Chinese Academy of Sciences
501 Haike Road
Shanghai 201203, PR China
E-mail: ypli@mail.shcnc.ac.cn
Dr. S. Zhang
Department of Radiology
Cancer Hospital/Institute & Department of Oncology
Shanghai Medical College
Fudan University
Shanghai 200032, PR China

DOI: 10.1002/adfm.201400256

the complex requirements in cancer therapy due to their well-defined nanoporous structures, tunable pore sizes, large surface area and abundant surface chemistry. Especially, the mesoporous channel combines the merits of enabling the high dispersion of large amounts of paramagnetic centers accessible for water molecules, and the encapsulation/sustained release of anti-cancer drugs.[7,9] Lin and co-workers grafted Gd chelates onto MSNs to fabricate hybrid mesoporous silica nanospheres (MSN-Gd) with high MRI performance.[7] Unfortunately, gadolinium-based MR CAs suffer from excreting from body through urine rapidly, having short circulating time as well as causing nephrogenic systemic fibrosis (NSF) especially for the patients with impaired kidney function as warned by U.S. Food and Drug Administration (FDA).[10] Therefore, seeking for new types of nanoprobes as T_1-positive MRI CAs to substitute for Gd-based T_1-MRI CAs has been urgently recommended and encouraged.

Our group recently developed a synthetic strategy of chemical oxidation/reduction reaction combined with heat treatment (O/R-HT) to fabricate manganese oxide/MSNs-based MRI-T_1 CAs by dispersing manganese oxide within mesopore channels of MSNs and their high performance for T_1-MRI has been well demonstrated both in vitro and in vivo.[11] However, Mn^{2+} suffers from the same toxicity issue as Gd^{3+}-based agents. Comparatively, Fe^{3+} is much more suitable for T_1-MRI based on the fact that iron species are rich in human blood in the form of ferritin.[6a] However, Fe species in the form of magnetic iron oxide NPs are typically used as T_2-weighted MRI CAs because these NPs exhibit the shortened relaxation time, e.g., enhanced r_2 value, resulting in a quick decrease in negative signal intensity.[12] Recently, it has been demonstrated that iron oxide NPs with ultrasmall sizes can be a good candidate as T_1 CAs.[5,13] Hyeon and co-workers synthesized extremely small-sized iron oxide NPs of <4 nm in size via the thermal decomposition of iron-oleate complex in the presence of oleyl alcohl, which shows the high T_1-MRI performances. It is considered that enhancing the accessibility of Fe paramagnetic centers to water molecules can improve their T_1-MRI performance.

Herein, we attempt to disperse ultrasmall iron oxide NPs within the well-defined mesopore channles of MSNs to take the advantage that mesopores can typically be employed as the nanoreactors to in-situ grow ultrasmall functional nanoparticles. Moreover, the remaining room within mesopore channels can be used as reservoirs for therapeutic agents. Importantly, the dispersed ultrasmall iron oxide NPs can interact with anticancer drug molecules by a special metal-ligand coordination bonding character, which can not only enhance the drug loading efficiency/amount, but can also enable intelligent coordination bond-based pH-responsive drug releases. Therefore, the ultrasmall iron oxide NPs-loaded MSNs can achieve the efficient T_1-MRI and the pH-responsive drug release features simultaneously. In addition, their special biological behaviors, such as the effect on the metastasis of cancer cells and reversing the multidrug resistance (MDR) of cancer cells, are also investigated in detail in this report.

2. Results and Discussion

As shown in **Scheme 1**a, the highly dispersed MCM-41-type MSNs with ordered mesopore channels were firstly synthesized by a typical sol-gel process based on soft-templating strategy, which provides an ideal matrix for the chemical vapor disposition of ferrocene within mesopores by a special

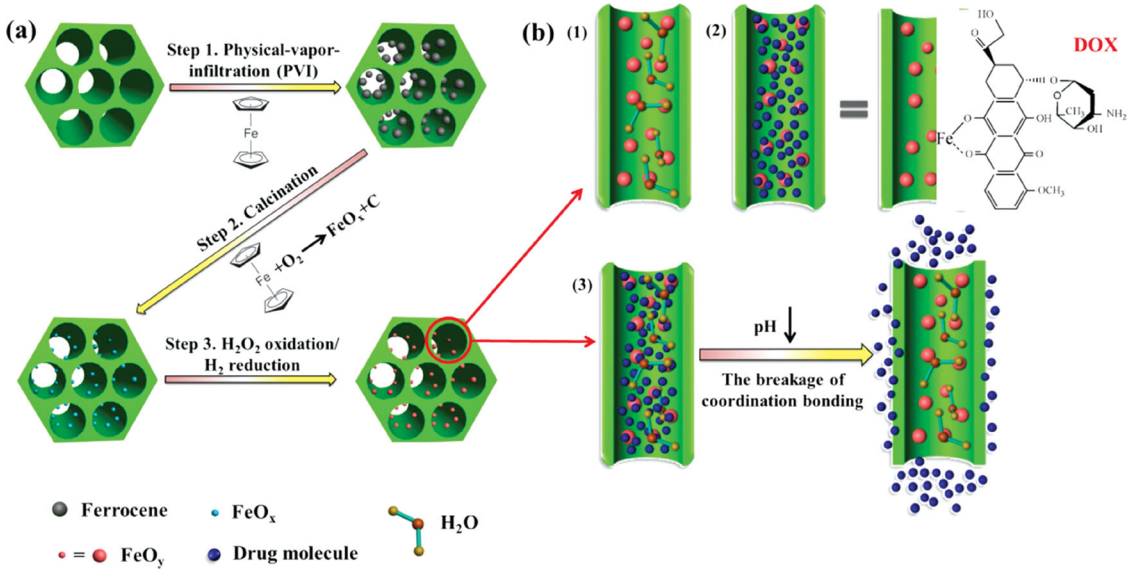

Scheme 1. (a) Schematic illustration of the formation of a ultrasmall iron oxide NPs-confined MSNs composite (Fe-MSNs). Ferrocene was first efficiently loaded within mesopores by a special PVI process (step 1), and the iron oxide NPs were in-situ generated after the decomposition of ferrocene (step 2). H_2O_2 treatment could enhance the hydrophilicity of Fe-MSNs, and the reduction process finally resulted in improved the T_1-MRI performance of composite NPs (step 3). (b) The roles of mesoporous channels in this theranostic system: (1) facilitating the free access of water molecules to paramagnetic Fe centers for enhanced T_1-MRI; (2) encapsulating anti-cancer drugs based on metal-ligand coordination bonding (DOX was chosen in this case) for pH-responsive DOX release.

physical-vapor-infiltration (PVI) method (step 1).[14] After the thermal treatment, the pre-introduced ferrocene in-situ decomposed into ultrasmall iron oxide NPs highly dispersed and confined within the mesopore channels. Especially, a H_2O_2 treatment upon as-obtained NPs endowed them with more hydrophilic groups (e.g., -COOH and -OH) to guarantee their high hydrophilicity.[15] The following heat treatment in reducing atmosphere (H_2/Ar) could further enhance the T_1-MRI relaxivity of iron oxide NPs confined within mesopores (designated as Fe-MSNs). The well-defined mesopore network favors the free accessibility of water molecules to magnetic centers for enhanced T_1-weighted MR relaxivity (Scheme 1b-1). The confined iron oxide NPs provide the anchoring sites for anticancer drug molecules via a special metal-ligand coordination bonding, which are sensitive to external pH variations (Scheme 1b-2).[16] It is noted that the encapsulation and pH-responsive anticancer drug release can reversibly change the interaction probability and bonding strength between Fe paramagnetic center and water molecules due to the shielding and exposure of the centers by the loaded drug molecules respectively before and after drug release, which can be potentially used for T_1-weighted MRI-guided monitoring of the drug release (Scheme 1b-3).

The morphology and microstructure of the as-synthesized MSNs and Fe-MSNs before and after H_2O_2 oxidation and H_2 reduction (H_2O_2-O/H_2-R) can be directly observed from transmission electron microscopy (TEM) and scanning electron microscopy (SEM) images (**Figure 1**a, b, c and S1). It can be found that both MSNs and Fe-MSNs exhibit and maintain uniform dimensions and spherical morphology during the synthesis (SEM), and well-defined two-dimensional hexagonally ordered mesoporous structure (TEM), though a number of small particles of iron oxide appear after the H_2O_2 oxidation and H_2 reduction. Comparatively, the mesopore regularity of Fe-MSNs are deteriorated after loading ferrocene, demonstrated by the reduced diffraction peak intensity in small-angle X-ray diffraction (SAXRD) and the disappearance of scattering ring in small-angle X-ray scattering (SAXS) (Figure S2).[17] Energy-dispersive X-ray spectroscopy (EDS) spectrum further demonstrates the presence of iron oxide NPs within MSNs (Figure S3). To further determine the dispersion status of iron oxides within mesopores, EDS element mapping was conducted (Figure $1a_3$-a_6, b_3-b_6 and c_3-c_6). The results show that iron species homogeneously distribute all over each MSN, which can be attributed to the homogeneous distribution of iron species within the mesopore network due to the confinement effect by the well-defined mesoporosity to the further growth of iron oxide NPs during PVI process. The Fe/Si atom ratio is 0.37:1 at 5 h of PVI and this ratio will increase with the extension time of PVI process. Such a high amount of iron oxide corresponds to the high encapsulation within the mesopore network, though small amount of iron oxide can be

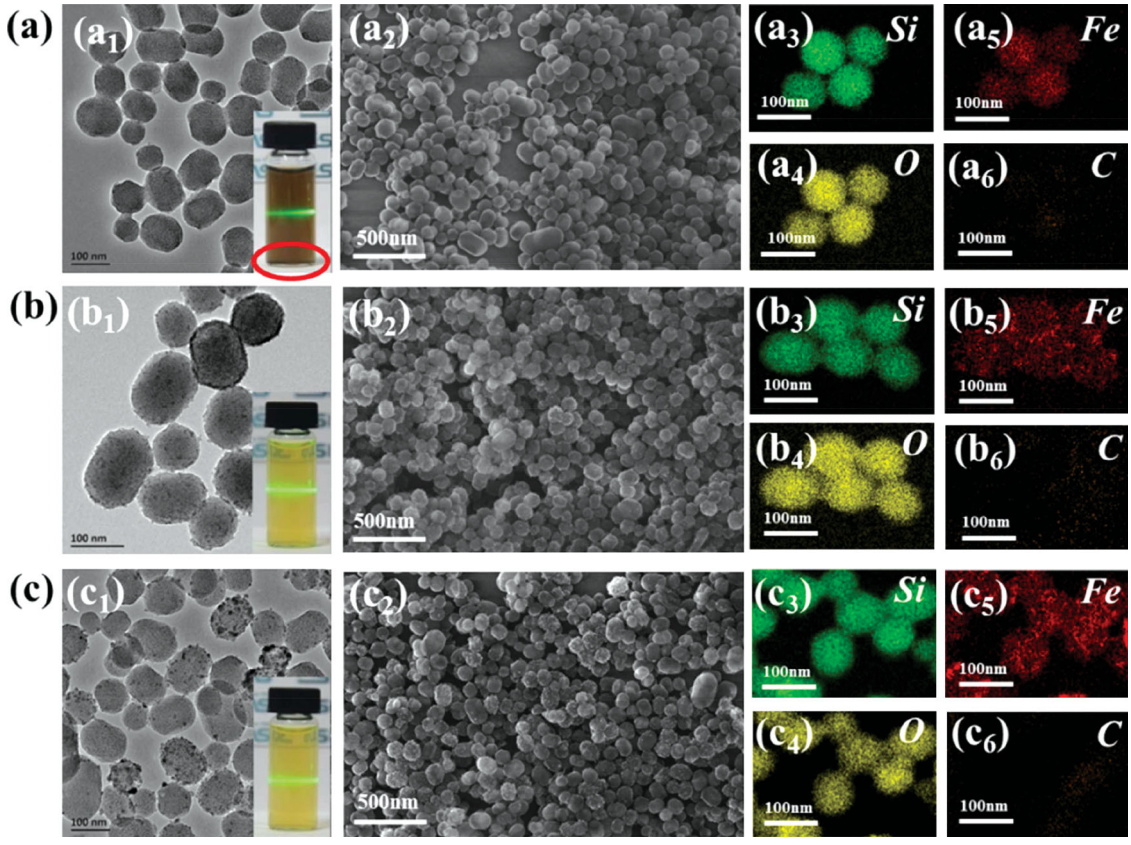

Figure 1. Structure and composition characterizations of Fe-MSNs before (a) and after (b) H_2O_2 oxidation, and further after H_2 reduction (c). TEM images are a_1, b_1 and c_1; SEM images are a_2, b_2 and c_2; The corresponding element mappings can be found in a_3-a_6, b_3-b_6 and c_3-c_6 (a_3, b_3 and c_3: Si; a_4, b_4 and c_4: O; a_5, b_5 and c_5: Fe; a_6, b_6 and c_6: C). Inset of a_1, b_1 and c_1 are the corresponding NP dispersions in aqueous solution.

found on the MSNs in Figure 1c$_1$. A few amount of carbon species can be found within Fe-MSNs before H_2O_2 oxidation (Figure 1a$_6$), which can cause slight precipitation of dispersed Fe-MSNs from the aqueous solution due to the relatively hydrophobic nature of generated carbon components (Figure 1a$_1$-inset). Importantly, the ordered mesostructure of Fe-MSNs can be well retained and carbon species can be hardly detected after further oxidation with H_2O_2 at room temperature. This process guarantees the high hydrophilicity and stability of Fe-MSNs in aqueous solution even after the thermal reduction process (Figure 1b and c). In addition, the average hydrated dynamic particle sizes of MSNs and Fe-MSNs before and after H_2O_2-O/H_2-R processes determined by dynamic light scattering (DLS, Figure S4a) are almost the same with each other (ca. 167 nm), demonstrating that such an iron oxide-loading process will not change the particle size of initial MSNs. The zeta potential of Fe-MSNs is approximately −43 mV (Figure S4b). The well-defined mesoporous structure of Fe-MSNs was further determined by the typical N_2 adsorption-desorption technique (Figure S4c, d) and the pore textual properties were listed in Table S1. The fabricated Fe-MSNs possess large surface area (557 m^2g^{-1}), high pore volume (0.49 cm^3g^{-1}) and 2.3 nm mesopore co-existing with 1.27 nm/1.48 nm micropores, which guarantees the further encapsulation and delivery of therapeutic agents.

The wide-angle X-ray diffraction (WAXRD) exhibit maghemite-Q (JCPDS 25–1402) patterns of Fe-MSNs after H_2O_2-O/H_2-R process (**Figure 2**a). It is clear that the Fe-MSNs are basically amorphous as can be understood from the very rough baselines in the patterns. Two very weak peaks for Fe-MSNs after H_2O_2-O/H_2-R can be found as circled, which can be indexed to γ-Fe_2O_3, corresponding to the small particles appeared on the surface of MSNs (Figure 1c$_1$). Nevertheless, it is believed that most of the iron species are still amorphous and encapsulated within the mesopore channels as suggested by the WAXRD patterns and elemental mapping results (Figure 1b$_5$ and c$_5$), considering the very high amount of iron oxide loading. In addition, the Fe-MSNs exhibit typical superparamagnetic properties as known from the absence of magnetic hysteresis loop (Figure 2b). It is known that magnetic properties are strongly dependent on the particle size.[6a,18] The low mass magnetization (M = 3.64 emu g^{-1}) of Fe-MSNs can be attributed to the ultrasmall-sized iron oxide NPs, which is in accordance with the results of TEM observations and EDS element mapping. From XPS analysis, the Fe 2p$_{3/2}$ spectra can be separated into two characteristic peaks at about 711 eV and 713 eV corresponding to Fe^{2+} and Fe^{3+}, respectively,[19] and the ratio of Fe^{2+}/Fe^{3+} increases after H_2 reduction (Figure 2c and d).

The synthesized Fe-MSNs after H_2O_2-O/H_2-R show the enhanced T_1-weighted signal with a r_1 value of 1.50 $mM^{-1}s^{-1}$ and r_2 value of 73.74 $mM^{-1}s^{-1}$, which are significantly higher than those before H_2O_2 oxidation (r_1: 0.11 $mM^{-1}s^{-1}$ and r_2: 5.18 $mM^{-1}s^{-1}$) and H_2 reduction (r_1: 0.33 $mM^{-1}s^{-1}$ and r_2: 12.33 $mM^{-1}s^{-1}$). This is mainly due to the lowered valence of Fe species under reducing atmosphere (e.g. Fe^{3+}-Fe^{2+} transformation) demonstrated by XPS analysis (**Figure 3**a and b). Furthermore, the Fe-MSNs were administrated into a mouse subcutaneously, and noninvasively traced with MRI at different intervals (Figure 3c) to preliminarily evaluate their in vivo performance.

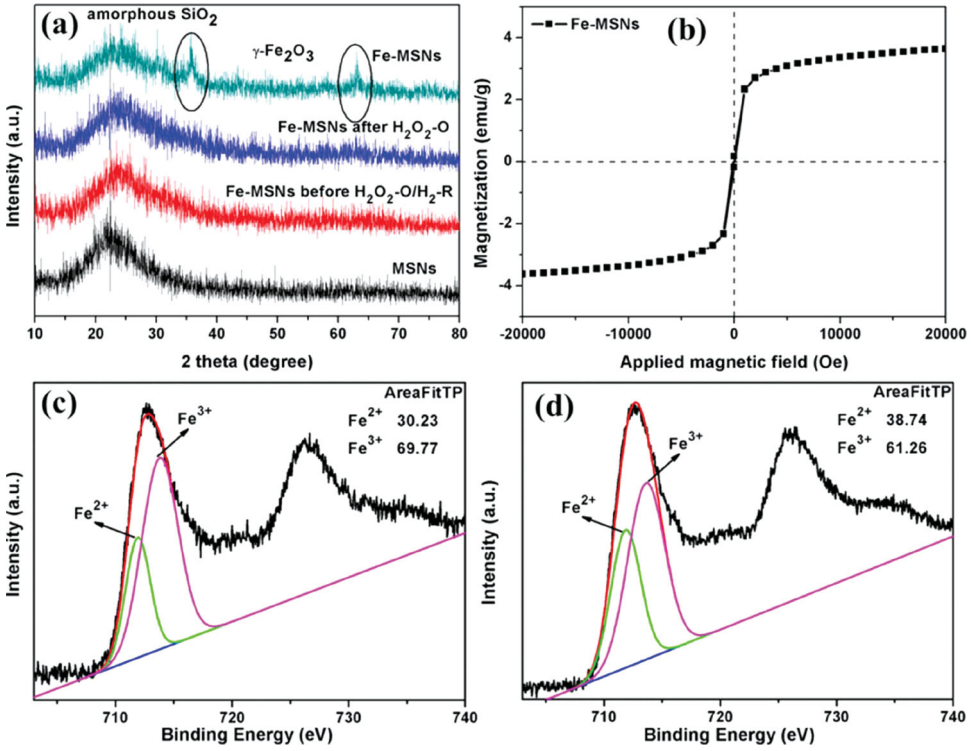

Figure 2. (a) Wide-angle X-ray diffraction patterns of MSNs and Fe-MSNs before and after H_2O_2 oxidation and H_2 reduction; (b) Field-dependent magnetization curve of Fe-MSNs measured at room temperature; XPS spectrum of Fe 2p$_{3/2}$ for Fe-MSNs before (c) and after (d) H_2O_2 oxidation and H_2 reduction.

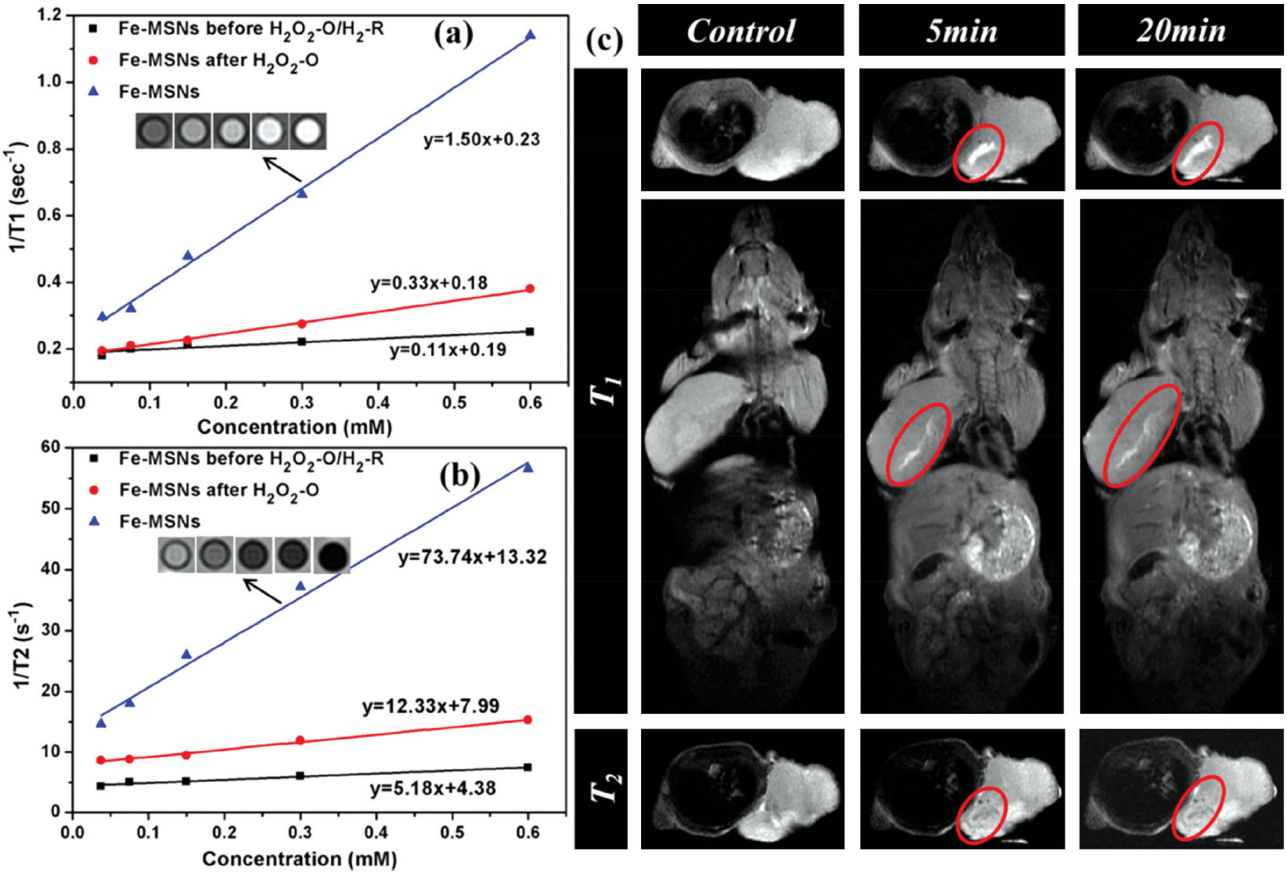

Figure 3. (a) T_1^{-1} and (b) T_2^{-1} versus Fe concentrations for Fe-MSNs before and after H_2O_2-O/H_2-R treatment. (c) In vivo MRI of a tumor-bearing mouse before and after the injection of Fe-MSNs for different time intervals.

The T_1-weighted images show that the positive signal intensities of tumor tissues increase significantly after the administration of Fe-MSNs and the bright region enlarges slowly within the tumor with the time prolongation of post-injection, while T_2-weighted images do not show significant changes after the injection, indicating that the obtained Fe-MSNs could be employed as an excellent T_1 CAs for MR imaging.

Importantly, Fe-MSNs provide an excellent platform for the loading and stimuli-responsive release of anti-cancer drugs due to the special interaction between Fe species evenly distributed within mesopores and anticancer drug molecules via metal ion-ligand coordination bonding.[16,20] The metal ion-ligand coordination bonding between solid-state metal ions and ligands has been demonstrated in metal oxide solids such as ZnO,[21] which, as we believe, might be also effective in the present case of iron oxides. Moreover, Fe species and protons are lewis acids while DOX is a lewis base, so such a bonding will be stable under physiological conditions but gradually cleaved under decreased pH environments due to the competitive behavior between Fe species and protons.[16b,20] This pH-sensitive drug releasing system is totally different from the typical on/off capping or gating approaches onto the surface of mesopores for pH-responsive drug release.[9b,22] The coordination bonding-based pH-responsive drug release was further demonstrated by employing two typical anticancer drugs, doxorubicin (DOX) and bleomycin (BLM), which possess amino, carbonyl and hydroxyl groups as binding sites to metal ions.[16b] As clearly shown in **Figure 4**a and b, the releases of DOX and BLM from Fe-MSNs are strongly dependent on the pH values. Only 14.4% of DOX and 8.3% of BLM have released under neutral conditions in 24 h, while lowering the pH value to 6.0 and 4.0, the 24 h-releasing amounts reach 28.6%, 67.2% for DOX and 61.4%, 79.6% for BLM, respectively. After replacing the releasing media of pH 7.4 with a buffer solution of pH 4.0 at 24 h, the additional 48 h-releasing amounts increase to 54.1% for DOX and 63.6% for BLM. The different release amounts of DOX and BLM under the same pH activation can be attributed to the different metal ion-ligand bonding characters between two types of drug molecules. To examine the feasibility of using Fe-MSNs as T_1-MRI CAs to monitor the release percentage of anti-cancer drugs in real-time, the longitudinal relaxation time periods of DOX-Fe-MSNs along with the DOX release from the carriers were measured. Accompanying the anti-cancer drug release from the carrier induced by the pH value decrease, the T_1-weighted MR image becomes brightened and relaxation time (T_1) shortened (i.e., r_1 value increase, Figure 4c). Correspondingly, in vivo T_1-MRI signals gradually become stronger at the tumor site after the intratumoral injection of DOX-Fe-MSNs (Figure 4d), which demonstrates that the coordination bonds between DOX and the carrier can be cleaved by the acidic environment in tumor regions, and more exposed Fe paramagnetic centers will become accessible to water molecules. This

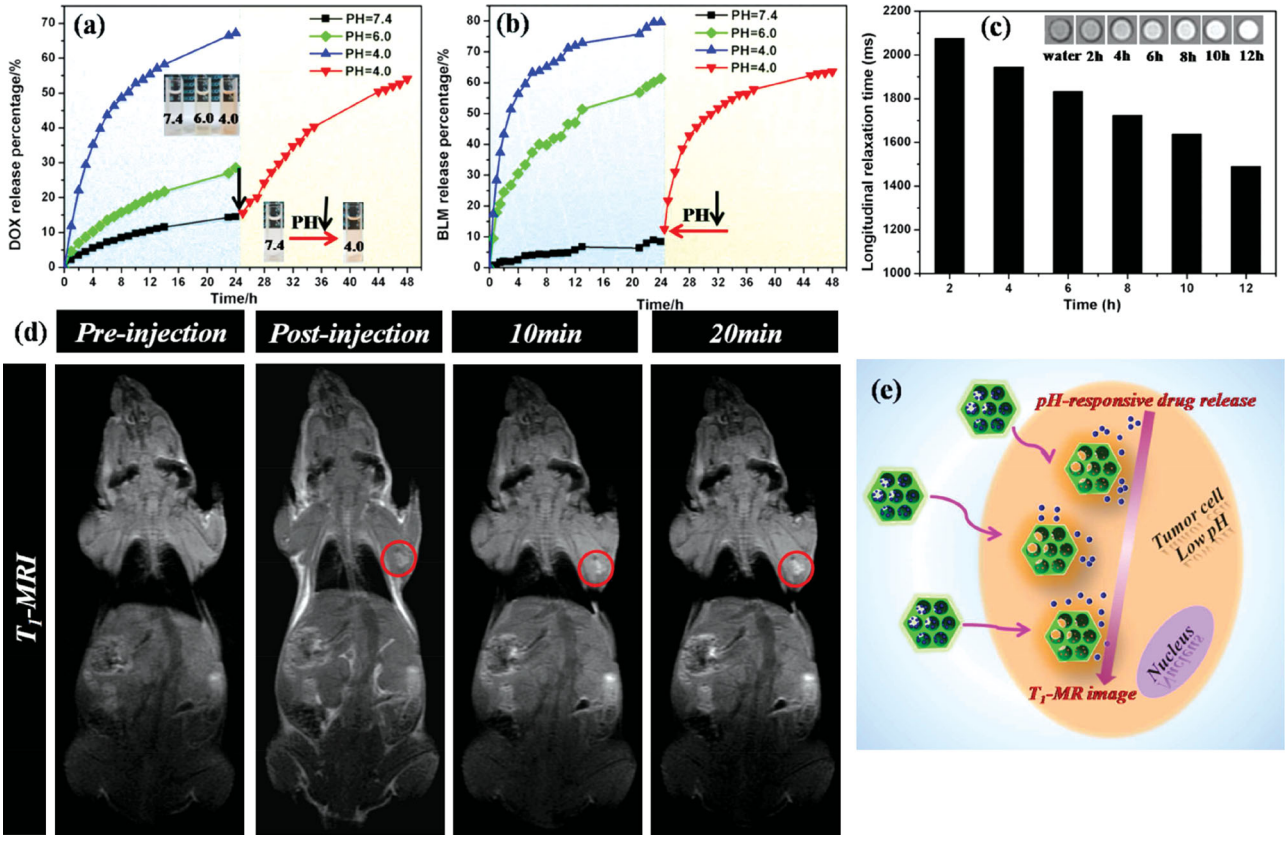

Figure 4. Release kinetics of anti-cancer drugs (a) DOX and (b) BLM from coordination bonding-based pH-responsive mesoporous carrier systems in buffer solutions of different pH values (7.4, 6.0 and 4.0). (c) Variations of longitudinal relaxation time durations along with the prolongation of DOX releasing from the carriers (inset: T_1-weighted MR images of the carries after DOX release). (d) In vivo T_1-MRI of a tumor-bearing mouse before and after the injection of DOX-Fe-MSNs for varied time durations. (e) Schematic illustration of pH-responsive drug release from Fe-MSNs-based theranostics under T_1 MRI-guidance. Anti-cancer drug releases from the carrier Fe-MSNs via the breakage of coordination bonds induced by intracellular acidic microenvironment in tumors.

conclusion is consistent with the in vitro results that the release of drug from Fe-MSNs could lead to the increase in the intensity of T_1 weighted MR image. This drug-release-induced T_1-MRI signal enhancement can be ascribed to facilitated access of more water molecules to the exposed iron paramagnetic centers after the pH-induced release of DOX molecules (Figure 4e).

The success of chemotherapy for cancer treatment is greatly limited by complex factors such as the multidrug resistance (MDR) and metastasis of cancer cells, which are among the most vital causes of chemotherapy failure and the high mortality of cancer patients.[23] The great efforts have been made to address these issues, but the poor bioavailability, high systemic toxicity and low efficacy of anticancer drugs still impose restrictions on further clinical development. It is important to note that the elaborately designed Fe-MSNs have been found to benefit the accumulation of drugs in tumors to circumvent MDR and suppress the migration and invasion of cancer cells.

The cytotoxicity assay of Fe-MSNs against MCF-7/ADR cancer cells at the concentrations of 12.5 to 600 μg mL^{-1} shows that Fe-MSNs will not cause the significant cytotoxicity to the cells even cultured for 48 h (**Figure 5**a), indicating their excellent biocompatibility. The cellular uptake of Fe-MSNs in MCF-7/ADR cells was investigated using red-emitting fluorescent dye, Rhodamine B isothiocyanate (RITC) labeled Fe-MSNs by flow cytometry (FCM) analysis (Figure 5b and c). It is found that large amounts of RITC-Fe-MSNs can be uptaken by cancer cells, which is strongly concentration- and time-dependent. The cellular uptake and intracellular location of RITC-Fe-MSNs were further observed by CLSM with the nuclei and lysosomes of cells stained by DAPI and Lyso Tracker Green DND-26 (Figure 5d), respectively. In 4 h of incubation, the strong red fluorescene of RITC-Fe-MSNs can be found co-localized with green lysotracker (yellow signal in Figure $5d_8$), indicating that Fe-MSNs NPs could enter lysosomes of MCF-7/ADR. However, these NPs cannot enter nuclei as demonstrated by the absence of red fluorescent signals of nanoparticles in nuclei (Figure $5d_4$ and d_9).

Importantly, free DOX exhibits higher cell viabilities than DOX-loaded Fe-MSNs after co-incubation with DOX-resistant MCF-7/ADR cells for 24 h and 48 h (**Figure 6**a) due to the limited cellular uptake of free DOX by MCF-7/ADR cells but substantially increased amounts of DOX within cells mediated by DOX-Fe-MSNs (Figure 6b and S5). The drug-resistance of cancer cells can be ascribed to the over-expression of multidrug efflux pumps P-glycoprotein (P-gp) that can pump out the free DOX molecules uptaken within cytoplasm.[24] It is noted that the expression of P-gp can be strongly inhibited after the uptake of Fe-MSNs, thus the MDR effect can be effectively reversed under the mediation by Fe-MSNs (Figure 6c). Importantly, Fe-MSNs demonstrate a special synergistic effect with

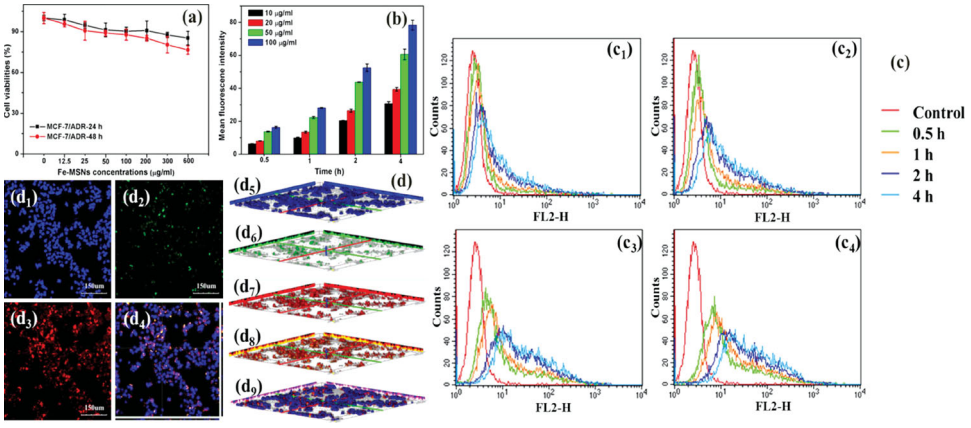

Figure 5. In vitro cytotoxicity and cellular uptake of RITC-Fe-MSNs. (a) Cell viabilities of Fe-MSNs against MCF-7/ADR at different concentrations in 24 and 48 h of incubation. (b-c) Amounts of RITC-Fe-MSNs uptaken in MCF-7/ADR in 0.5, 1, 2 and 4 h of incubation (c_1: 10 μg mL^{-1}; c_2: 20 μg mL^{-1}; c_3: 50 μg mL^{-1}; c_4: 100 μg mL^{-1}L) determined by flow cytometry. CLSM images (d_{1-4}) of MCF-7/ADR cells after co-incubation with RITC-Fe-MSNs (50 μg mL^{-1}) for 4 h. After incubation, the cell nuclei were stained with DAPI and lysosomes were stained with Lyso Tracker Green DND-26; Three-dimensional confocal fluorescene reconstructions (d_5-d_9) of nanoparticles endocytosed MCF-7/ADR cells to demonstrate the internalization and intracellular locations of NPs within cancer cells (nuclei (d_1, d_5): blue fluorescene of DAPI staining; lysosomes (d_2, d_6): green fluorescene of Lyso Tracker Green DND-26 staining; Fe-MSNs (d_3, d_7): red fluorescene of RITC grafting).

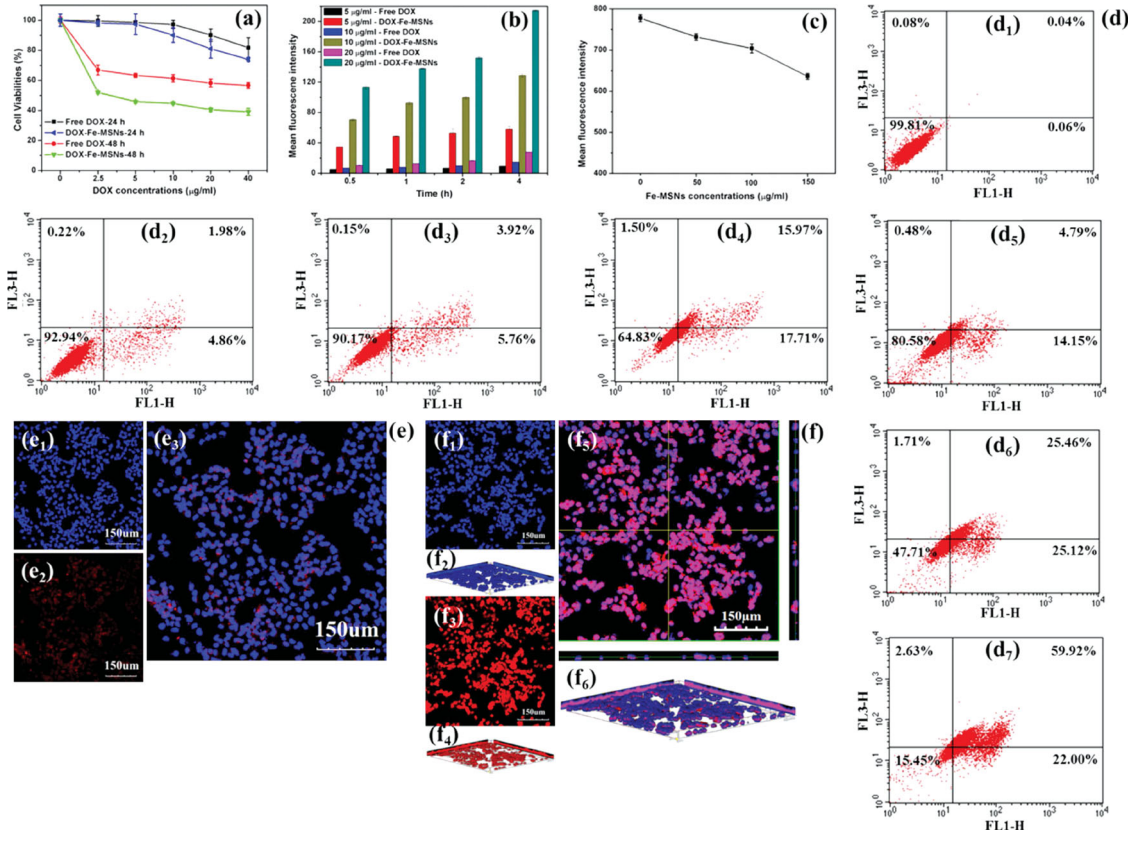

Figure 6. (a) Cell viabilities of free DOX and DOX-Fe-MSNs against MCF-7/ADR at different DOX concentrations in 24 and 48 h of incubation. (b) Celluar uptake amounts of free DOX and DOX-Fe-MSNs on MCF-7/ADR with different concentrations of DOX (5 μg mL^{-1}; 10 μg mL^{-1} and 20 μg mL^{-1}) in 0.5, 1, 2 and 4 h of incubation. (c) P-gp expressions on MCF-7/ADR at different concentrations of Fe-MSNs (50; 100; 150 μg mL^{-1}) in 48 h of incubation. (d) Cell apoptosis of MCF-7/ADR by different treatments for 48 h (d_1: control; d_2: free DOX (5 μg mL^{-1}); d_3: free DOX (10 μg mL^{-1}); d_4: free DOX (20 μg mL^{-1}); d_5: DOX-Fe-MSNs ([DOX] = 5 μg mL^{-1}); d_6: DOX-Fe-MSNs ([DOX] = 10 μg mL^{-1}); d_7: DOX-Fe-MSNs ([DOX] = 20 μg mL^{-1})). CLSM images of MCF-7/ADR cells incubated with Free DOX (e) and DOX-loaded Fe-MSNs (f) ([DOX] = 10 μg mL^{-1}) for 4 h. After incubation, the cell nuclei were stained with DAPI; Three-dimensional confocal fluorescene reconstructions (f_2, f_4 and f_6) of MCF-7/ADR cells after uptaking DOX-Fe-MSNs to directly observe intracellular delivery of DOX by Fe-MSNs drug vehicles (e_1, f_1, f_2: blue channel; e_2, f_3, f_4: red channel; e_3, f_5, f_6: merged image of e_1 and e_2, f_1 and f_3, f_2 and f_4, respectively).

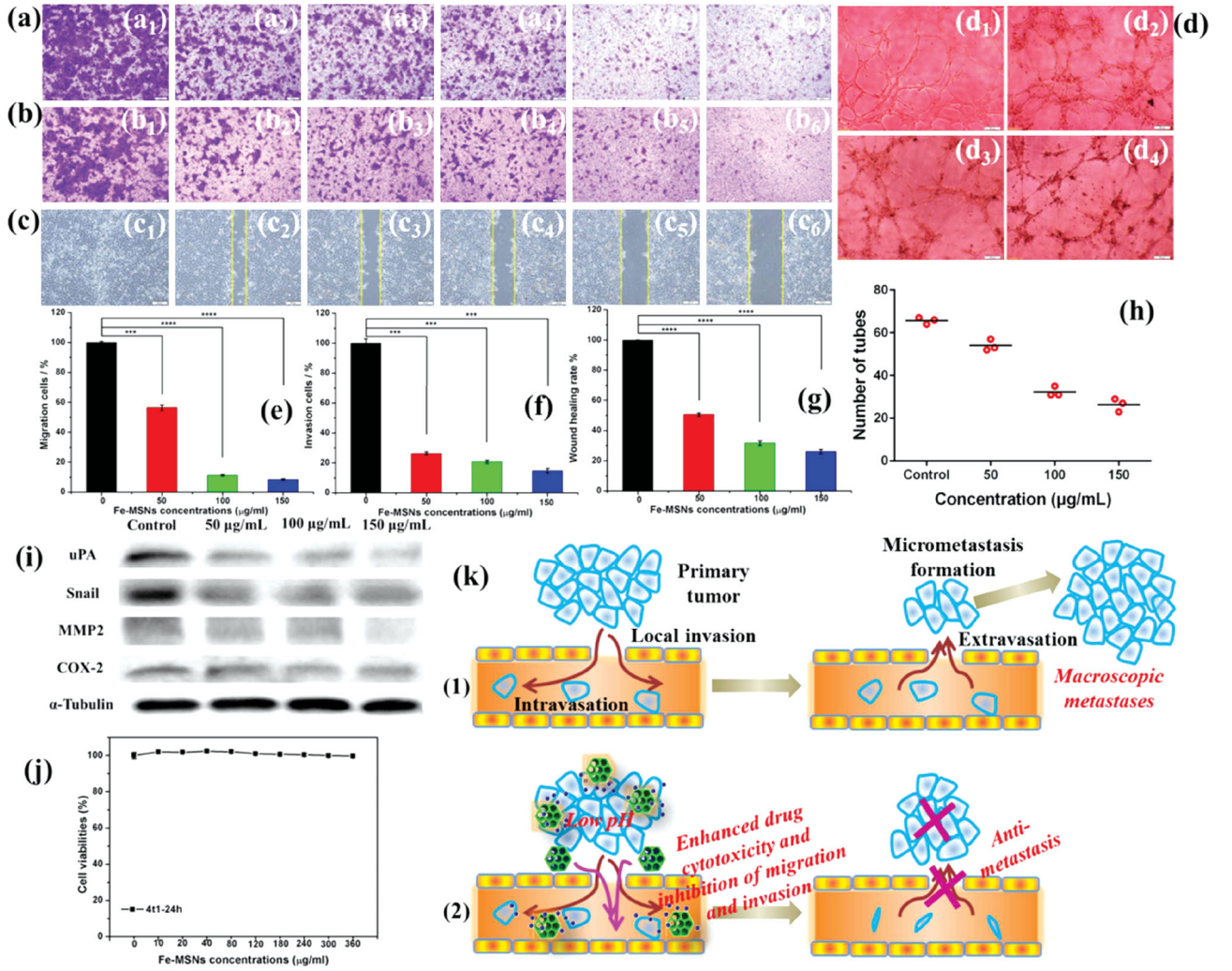

Figure 7. In vitro (a) migration, (b) invasion,(c) wound healing and (d) tube formation assays. Representative microscopic fields of 4T1 cells after treatments with Fe-MSNs of varied concentrations (a_1, b_1, c_1 and d_1: control; a_2, b_2 and c_2:15 μg mL^{-1}; a_3, b_3 and c_3: 25 μg mL^{-1}; a_4, b_4, c_4 and d_2: 50 μg mL^{-1}; a_5, b_5, c_5 and d_3: 100 μg mL^{-1}; a_6, b_6, c_6 and d_4: 150 μg mL^{-1}). The scale bars in a, b, c and d are 200 μm. Percentages of migrated (e, ***p < 0.001, ****p < 0.0001), invasive (f, ***p < 0.001) cancer cells and cell wound healing rate (g, ****p < 0.0001), and the number of tubes (h) with different treatments. (i) Inhibitory effects of Fe-MSNs with varied concentrations on the expression of uPA, Snail, MMP2 and COX-2 determined by Western blotting analysis. (j) 4T1 cell viabilities treated with Fe-MSNs at varied concentrations in 24 h of incubation. (k) Schematic illustration of cancer cell metastasis (1) and the simultaneous anti-metastasis and enhanced drug cytotoxicity by DOX-Fe-MSNs (2).

DOX on promoting cell apoptosis, resulting in significantly increased cell apoptosis compared with free DOX-treated cells (Figure 6d). CLSM was also used to observe the internalization of DOX-Fe-MSNs into MCF-7/ADR and intracellular release of DOX. Compared with free DOX (Figure 6e), DOX accumulation within cancer cells can be much enhanced under the Fe-MSN mediation (Figure 6f and S6), which is consistent with quantitative FCM analysis (Figure 6b and S5).

Metastasis is a formidable process leading to high mortality of cancer sufferers, which involves the primary tumor cell invading to the adjacent tissue-invasion, entering boold circulation stream-intravasation, extravasating through the capillary endothelium at distal sites-extravasation, forming micrometastasis and proliferating to macroscopic metastases (**Figure 7**k-1).[25] The biological effect of Fe-MSNs on the migration and invasion behavior of cancer cells was systematically investigated by using highly metastatic 4T1 breast cancer cellss at varied Fe-MSNs concentrations (15, 25, 50, 100 and 150 μg mL^{-1}). The qualitative and quantitative results show that 4T1 cells after the pre-treatments with different concentrations of Fe-MSNs significantly depress their migration and invasion, which are highly concentration-dependent (Figure 7a, b, e and f). The cell wound healing assay in 24 h after scratched (Figure 7c) show that wound healing area scarcely exists in cells pre-incubated with different concentrations of Fe-MSNs compared with untreated cells that heal completely, and the wound healing rate is only 26.1% of control group at the Fe-MSNs concentration of 150 μg mL^{-1} (Figure 7g). Moreover, angiogenesis is another key factor for tumor growth and metastasis, and the development of angiogenesis inhibitors is very important for inhibiting cancer growth. Interestingly, only few capillary tubes are visible, and no formation of cellular networks is in sight after treatments

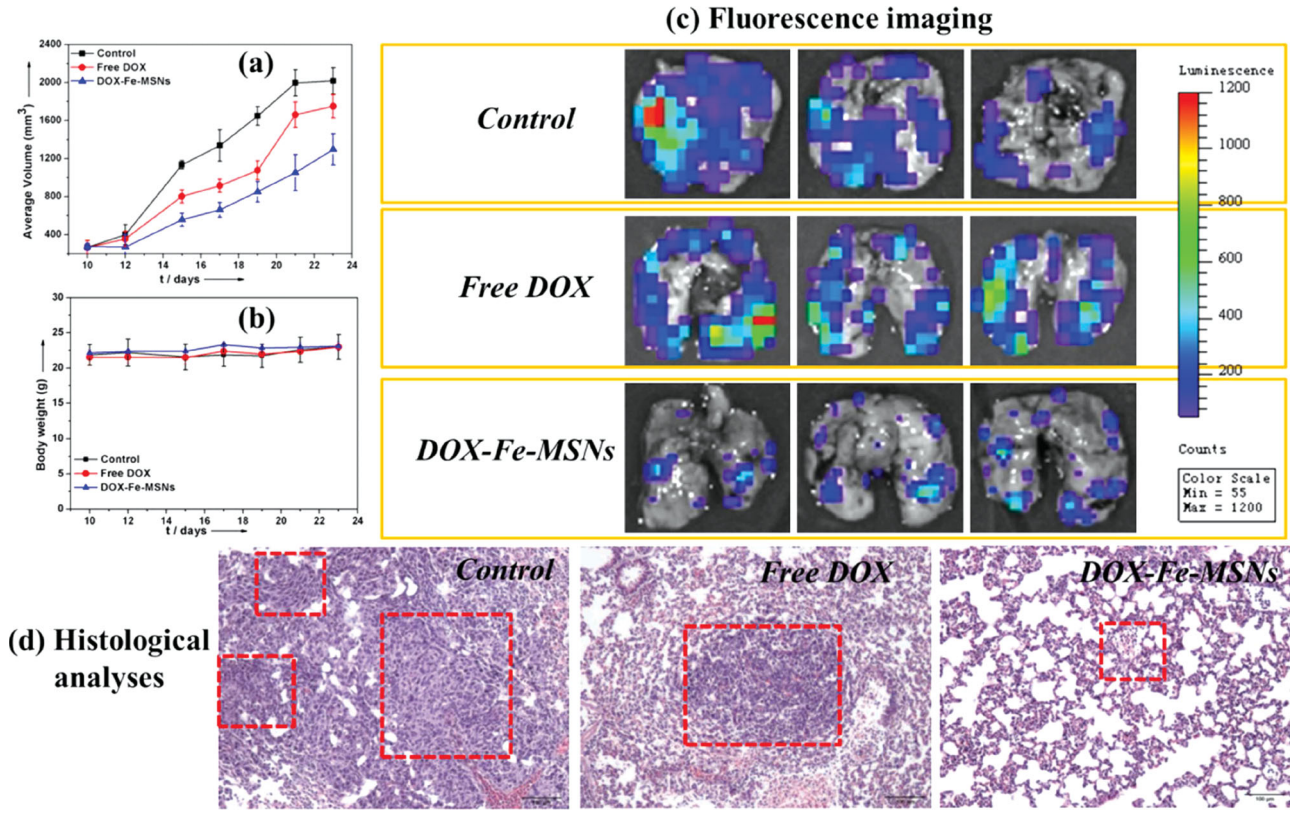

Figure 8. In vivo therapeutic effects of DOX-loaded Fe-MSNs on 4T1 pulmonary metastatic mice model. Antitumor effects (a) and body weight changes (b) of tumor-bearing femal mice (n = 5) treated with saline, free DOX and DOX-Fe-MSNs (DOX doses: 2.5 mg kg^{-1}) twice for 23 days. Ex vivo fluorescence imagings of excised lung tissues (c) and histological analyses of breast cancer pulmonary metastases (d) after treatments with saline, free DOX and DOX-Fe-MSNs. The scale bars of d are 100 μm.

with Fe-MSNs, demonstrating that Fe-MSNs can disrupt the enclosed capillary networks formed by human microvascular endothelial cells (HMEC-1) (Figure 7d and h). Cell migration, invasion and tube formation processes are regulated by numerous gene products including urinary plasminogen activator (uPA), Snail, matrix metalloproteinase 2 (MMP2) and cyclooxygenase 2 (COX-2) and other chemokines.[26] Notably, the expressions of these proteins in the 4T1 cells co-incubated with Fe-MSNs are significantly down-regulated with a concentration-dependent character (Figure 7i), which means that Fe-MSNs have significant inhibitory effect on the metastasis of metastatic cancer cells by down-regulating the expressions of metastasis-related proteins, consistent with the previous reports about the metastasis inhibition of cancer cells using engineered NPs by so-called imprisoning instead of poisoning cancer cells.[27] Additionally, Fe-MSNs show negligible cytotoxicity against 4T1 cells (Figure 7j) but can effectively suppress the dissemination of breast cancer cells (Figure 7k-2).

The relatively long term in vivo histocompatibility of Fe-MSNs was recorded after intravenous injection of Fe-MSNs in mice with different doses (0, 25, 50 and 100 mg kg^{-1}) for 15 and 30 days. No apparent pathological changes in the main tissues (heart, liver, spleen, lung and kidney) along with the increase of dosages and time (Figure S7 and S8) could be observed from the histological hematoxylin-eosin (HE) results, demonstrating that the Fe-MSNs possess the high tissue biocompatibility. Furthermore, the 4T1 pulmonary metastatic mice model was employed to assess the effectiveness of DOX-loaded Fe-MSNs in inhibiting the growth and metastasis of the tumor in vivo. It is found that the average tumor volumes of the mice treated with free DOX and DOX-Fe-MSNs are 86.7% and 64.2% of saline group, respectively (**Figure 8**a), which is consistent with the results of in vitro cytotoxicity and demonstrates the effectively enhanced drug bioavailability and tumoricidal efficiency by Fe-MSNs-mediated DOX delivery. The body weight changes in all groups, as an indicator of systemic toxicity, were measured simultaneously (Figure 8b). The results show that no distinct body weight changes occur, indicating slight systemic toxicity of the nanomedicine. The in vivo anti-metastatic efficacy of Fe-MSNs was further evaluated by bioluminescence imaging (BLI) of pulmonary metastatic nodules, which were formed by the metastasis of 4T1-luciferase mammary tumor cells (Figure 8c). The bioluminescence intensity indicates the numbers of metastatic cancer cells. It is noted that DOX-Fe-MSNs can significantly inhibit the formation of lung metastases compared with control group. In contrast, the inhibitory effect of free DOX is obviously lower. The HE staining images of the lung tissues also demonstrate the remarkably more efficient suppression of tumor metastases by the treatment of DOX-Fe-MSNs, in comparison with free DOX group (Figure 8d). This could be attributed to the enhanced drug delivery and bioavailability of anticancer drug DOX, and thus leading to significantly enhanced

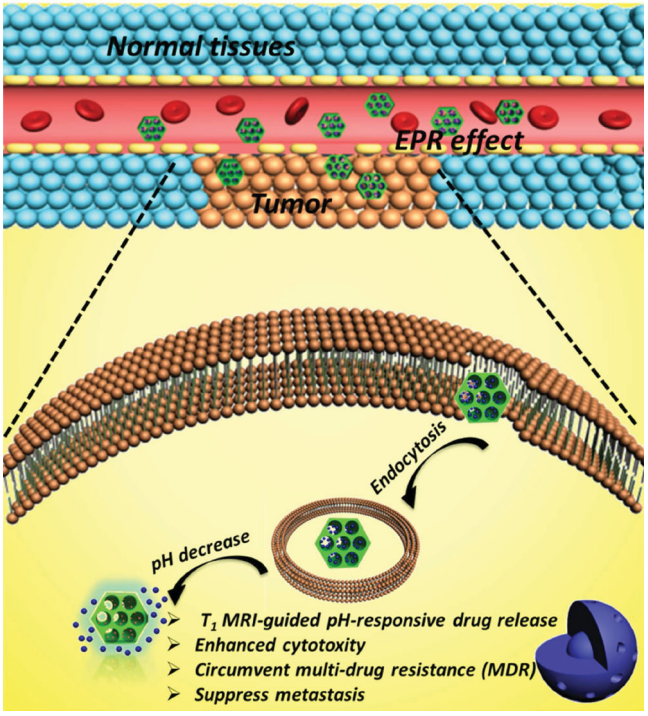

Scheme 2. Strategy schematics of Fe-MSNs-based anti-cancer nanotheranostics for concurrent T_1-weighted MR imaging and pH-responsive drug release, which will benefit the enhanced therapeutic efficacy by Fe-MSNs-mediated drug endocytosis, decreased efflux pump effect for anti-MDR and depressed migration and invasion for anti-metastasis of cancer cells.

chemotherapeutic efficiency. These results demonstrate that DOX-loaded Fe-MSNs can not only inhibit the in situ tumor growth, but also suppress the in vivo pulmonary metastasis of 4T1 cells effectively.

3. Conclusion

A highly efficient theranostic platform based on MSNs with ultrasmall iron oxide NPs confined within mesopore network has been designed and synthesized by a facile but efficient physical-vapor-infiltration (PVI) method. The nanosized Fe-MSNs can transport through the blood vessels and accumulate within tumor tissues by the typical enhanced permeability and retention (EPR) effect (**Scheme 2**), while the highly dispersed ultrasmall iron oxide NPs within mesopore channels can function as the CAs for efficient T_1-weighted MR imaging in vitro and in vivo. Importantly, the unique metal-ligand coordiation bonding between Fe species and anticancer drug molecules endows the carrier with a pH-responsive drug release feature, by which the drugs can be released from the carrier when they reach the tumor tissues and are endocytosed into cancer cells/organelles of low pH values. Especially, the gradual iron paramagnetic centers' exposure along with the drug release from the mesopore channels enables excellent and synchronously intensified T_1-MR imaging of the nanomedicine, which facilitates the real time monitoring of the release of anticancer drugs in the regions of interests. Moreover, the uptake of biocompatible Fe-MSNs can significantly inhibit the metastasis of cancer cells by down-regulating the metastasis-related proteins (e.g., uPA, MMP2 and COX-2), and the anticancer drug-loaded carrier can reverse the MDR of cancer cells by suppressing the drug efflux pump effect by P-gp in cells. Therefore, the proposed Fe-MSNs-based theranostic platform is expected to significantly extend the biomedical applications of MSNs-based nanotheranostics based on its special biological effects and excellent properties, and therefore holds the great potential for further clinical translations and applications.

Supporting Information

Supporting Information is available from the Wiley Online Library or from the author.

Acknowledgements

W. and Q.M. contributed equally to this work. The authors gratefully acknowledge the support of this research by National Key Basic Research Program of China (973 Program, Grant No. 2011CB707905 and 2010CB934000), National Nature Science Foundation of China (Grant No. 51302293, 51132009, 51072212, 81270047, 21177137), China National Funds for Distinguished Young Scientists (Grant No. 51225202), National Natural Science Foundation of Shanghai (Grant No. 11nm0506500) and Foundation for Youth Scholar of State Key Laboratory of High Performance Ceramics and Superfine Microstructures (Grant No. SKL201203).

Received: January 23, 2014
Published online: April 4, 2014

[1] a) F. M. Kievit, M. Zhang, *Adv. Mater.* **2011**, *23*, H217; b) M. P. Melancon, R. J. Stafford, C. Li, *J. Controlled Release* **2012**, *164*, 177; c) T. Lammers, F. Kiessling, W. E. Hennink, G. Storm, *Mol. Pharm.* **2010**, *7*, 1899.
[2] a) I. Mellman, R. Fuchs, A. Helenius, *Annu. Rev. Biochem* **1986**, *55*, 663; b) I. F. Tannock, D. Rotin, *Cancer Res.* **1989**, *49*, 4373.
[3] T. D. Nguyen, Y. Liu, S. Saha, K. C. F. Leung, J. F. Stoddart, J. I. Zink, *J. Am. Chem. Soc.* **2007**, *129*, 626.
[4] Q. Fu, G. V. R. Rao, L. K. Ista, Y. Wu, B. P. Andrzejewski, L. A. Sklar, T. L. Ward, G. P. Lopez, *Adv. Mater.* **2003**, *15*, 1262.
[5] E. Taboada, E. Rodríguez, A. Roig, J. Oró, A. Roch, R. N. Muller, *Langmuir* **2007**, *10*, 4583.
[6] a) B. H. Kim, N. Lee, H. Kim, K. An, Y. I. Park, Y. Choi, K. Shin, Y. Lee, S. G. Kwon, H. B. Na, J. G. Park, T. Y. Ahn, Y. W. Kim, W. K. Moon, S. H. Choi, T. Hyeon, *J. Am. Chem. Soc.* **2011**, *133*, 12624; b) R. Guillet Nicolas, J. L. Bridot, Y. Seo, M. A. Fortin, F. Kleitz, *Adv. Func. Mater.* **2011**, *21*, 4653; c) S. L. Pinho, H. Faneca, C. F. Geraldes, M. H. Delville, L. D. Carlos, J. Rocha, *Biomaterials* **2012**, *33*, 925; d) T. Kim, E. Momin, J. Choi, K. Yuan, H. Zaidi, J. Kim, M. Park, N. Lee, M. T. McMahon, A. Quinones Hinojosa, J. W. M. Bulte, T. Hyeon, A. A. Gilad, *J. Am. Chem. Soc.* **2011**, *133*, 2955; e) H. B. Na, J. H. Lee, K. An, Y. I. Park, M. Park, I. S. Lee, D. H. Nam, S. T. Kim, S. H. Kim, S. W. Kim, K. H. Lim, K. S. Kim, S. O. Kim, T. Hyeon, *Angew. Chem. Int. Ed.* **2007**, *46*, 5397.
[7] K. M. Taylor, J. S. Kim, W. J. Rieter, H. An, W. Lin, W. Lin, *J. Am. Chem. Soc.* **2008**, *130*, 2154.
[8] a) M. K. Yu, D. Kim, I. H. Lee, J. S. So, Y. Y. Jeong, S. Jon, *Small* **2011**, *7*, 2241; b) Y. J. Chang, C. H. Chang, C. Y. Yu, T. J. Chang, L. C. Chen, M. H. Chen, T. W. Lee, G. Ting, *Nucl. Med. Biol* **2010**, *37*, 95; c) V. Krishna, A. Singh, P. Sharma, N. Iwakuma, Q. Wang, Q. Zhang, J. Knapik, H. Jiang, S. R. Grobmyer, B. Koopman, B. Moudgil, *Small* **2010**, *6*, 2236.

[9] a) S. Li, H. liu, L. Li, N. Q. Luo, R. H. Cao, D. H. Chen, Y. Z. Shao, *Appl. Phys. Lett.* **2011**, *98*, 093704; b) Y. Zhu, J. Shi, W. Shen, X. Dong, J. Feng, M. Ruan, Y. Li, *Angew. Chem. Int. Ed.* **2005**, *44*, 5083; c) Y. Chen, H. Chen, L. Guo, Q. He, F. Chen, J. Zhou, J. Feng, J. Shi, *ACS Nano* **2009**, *4*, 529; d) Y. Chen, H. Chen, D. Zeng, Y. Tian, F. Chen, J. Feng, J. Shi, *ACS Nano* **2010**, *4*, 6001.

[10] J. G. Penfield, R. F. Reilly Jr., *Nat. Clin. Pract. Nephr.* **2007**, *3*, 654.

[11] Y. Chen, H. Chen, S. Zhang, F. Chen, S. Sun, Q. He, M. Ma, X. Wang, H. Wu, L. Zhang, L. Zhang, J. Shi, *Biomaterials* **2012**, *33*, 2388.

[12] a) S. Tong, S. Hou, Z. Zheng, J. Zhou, G. Bao, *Nano Lett.* **2010**, *10*, 4607; b) D. A. J. Herman, P. Ferguson, S. Cheong, I. F. Hermans, B. J. Ruck, K. M. Allan, S. Prabakar, J. L. Spencer, C. D. Lendrum, R. D. Tilley, *Chem. Commun.* **2011**, *47*, 9221.

[13] a) C. H. Cunningham, T. Arai, P. C. Yang, M. V. McConnell, J. M. Pauly, S. M. Conolly, *Mag. Reson. Med.* **2005**, *53*, 999; b) A. Roch, R. N. Muller, P. Gillis, *J. Chem. Phys.* **1999**, *110*, 5403; c) F. Hu, Q. Jia, Y. Li, M. Gao, *Nanotechnology* **2011**, *22*, 245604; d) Ulrich I. Tromsdorf, Oliver T. Bruns, Sunhild C. Salmen , Ulrike Beisiegel, H. Weller, *Nano Lett.* **2009**, *9*, 4434.

[14] L. X. Zhang, Z. L. Hua, X. P. Dong, L. Li, H. R. Chen, J. L. Shi, *J. Mol. Catal. A: Chem.* **2007**, *268*, 155.

[15] a) B. Chang, J. Fu, Y. Tian, X. Dong, *J. Phys. Chem. C* **2013**, *117*, 6252; b) D. Giasafaki, A. Bourlinos, G. Charalambopoulou, A. Stubos, T. Steriotis, *Microporous Mesoporous Mater.* **2012**, *154*, 74.

[16] a) H. Zheng, S. Che, *RSC Adv.* **2012**, *2*, 4421; b) H. Zheng, L. Xing, Y. Cao, S. Che, *Coord. Chem. Rev.* **2013**, *257*, 1933.

[17] a) Y. Deng, T. Yu, Y. Wan, Y. Shi, Y. Meng, D. Gu, L. Zhang, Y. Huang, C. Liu, X. Wu, D. Zhao, *J. Am. Chem. Soc.* **2007**, *129*, 1690; b) T. R. Pauly, Y. Liu, T. J. Pinnavaia, S. J. L. Billinge, T. P. Rieker, *J. Am. Chem. Soc.* **1999**, *121*, 8835.

[18] a) R. W. Chantrell, J. Popplewell, S. W. Charles, *IEEE Trans. Magn.* **1978**, *MAG-14*, 975; b) A. G. Roca, J. F. Marco, M. d. P. Morales, C. J. Serna, *J. Phys. Chem. C* **2007**, *111*, 18577.

[19] a) Z. H. Chen, F. R. Wang, H. Li, Q. Yang, L. F. Wang, X. H. Li, *Ind. Eng. Chem. Res.* **2012**, *51*, 202; b) J. R. Scheffe, A. Frances, D. M. King, X. H. Liang, B. A. Branch, A. S. Cavanagh, S. M. George, A. W. Weimer, *Thin Solid Films* **2009**, *517*, 1874.

[20] H. Zheng, Y. Wang, S. Che, *J. Phys. Chem. C* **2011**, *115*, 16803.

[21] K. C. Barick, S. Nigam, D. Bahadur, *J. Mater. Chem.* **2010**, *20*, 6446.

[22] a) C. Park, K. Oh, S. C. Lee, C. Kim, *Angew. Chem. Int. Ed.* **2007**, *46*, 1455; b) E. Aznar, M. D. Marcos, R. Martinez-Manez, F. Sancenon, J. Soto, P. Amoros, C. Guillem, *J. Am. Chem. Soc.* **2009**, *131*, 6833; c) S. Angelos, N. M. Khashab, Y.-W. Yang, A. Trabolsi, H. A. Khatib, J. F. Stoddart, J. I. Zink, *J. Am. Chem. Soc.* **2009**, *131*, 12912.

[23] a) A. M. Gonzalez-Angulo, F. Morales-Vasquez, G. N. Hortobagyi, *Adv. Exp. Med. Biol.* **2007**, *608*, 1–22; b) C. Bock, T. Lengauer, *Nat. Rev. Cancer* **2012**, *12*, 494; c) B. L. Eckhardt, P. A. Francis, B. S. Parker, R. L. Anderson, *Nat Rev Drug Discov.* **2012**, *11*, 479; d) A. F. Chambers, I. C. MacDonald, E. E. Schmidt, S. Koop, V. L. Morris, R. Khokha, A. C. Groom, *Cancer Metastasis Rev.* **1995**, *14*, 279.

[24] S. M. He, R. Li, J. R. Kanwar, S. F. Zhou, *Curr. Med. Chem.* **2011**, *18*, 439.

[25] J. Yang, S. A. Mani, J. L. Donaher, S. Ramaswamy, R. A. Itzykson, C. Come, P. Savagner, I. Gitelman, A. Richardson, R. A. Weinberg, *Cell* **2004**, *117*, 927.

[26] a) P. Anand, A. B. Kunnumakkara, K. B. Harikumar, K. S. Ahn, V. Badmaev, B. B. Aggarwal, *Cancer Res.* **2008**, *68*, 8861; b) T. Joki, O. Heese, D. C. Nikas, L. Bello, J. Zhang, S.-K. Kraeft, N. T. Seyfried, T. Abe, L. B. Chen, R. S. Carroll, P. M. Black, *Cancer Res.* **2000**, *60*, 4926.

[27] a) H. Meng, G. Xing, E. Blanco, Y. Song, L. Zhao, B. Sun, X. Li, P. C. Wang, A. Korotcov, W. Li, X. J. Liang, C. Chen, H. Yuan, F. Zhao, Z. Chen, T. Sun, Z. Chai, M. Ferrari, Y. Zhao, *Nanomedicine* **2012**, *8*, 136; b) H. Meng, G. Xing, B. Sun, F. Zhao, H. Lei, W. Li, Y. Song, Z. Chen, H. Yuan, X. Wang, J. Long, C. Chen, X. Liang, N. Zhang, Z. Chai, Y. Zhao, *ACS Nano* **2010**, *4*, 2773.